

Research paper

Seeing beyond the outcrop: Integration of ground-penetrating radar with digital outcrop models of a paleokarst system

Julian Janocha^{a,b,c,*}, Aleksandra Smyrak-Sikora^a, Kim Senger^a, Thomas Birchall^{a,d}^a Department of Arctic Geology, The University Centre in Svalbard, PO Box 156, 9171 Longyearbyen, Norway^b Department of Geosciences, University of Tromsø – The Arctic University of Norway, P.O. Box 6050, Langnes, 9037 Tromsø, Norway^c Institute for Geosciences, University of Potsdam, Karl-Liebknecht-Strasse 24-25, 14476 Potsdam, Germany^d Department of Geosciences, University of Oslo, P.O. Box 1047, Blindern, 0316 Oslo, Norway

ARTICLE INFO

Keywords:

Digital geology
Svalbard
Billefjorden trough
Upper Paleozoic
Fortet member
Dissolution collapse breccia
Syn-rift breccia

ABSTRACT

Paleokarst breccias are a common feature of sedimentary rift basins. The Billefjorden Trough in the High Arctic archipelago of Svalbard is an example of such a rift. Here the Carboniferous stratigraphy exhibits intervals of paleokarst breccias formed by gypsum dissolution. In this study we integrate digital outcrop models (DOMs) with a 2D ground penetrating radar (GPR) survey to extrapolate external irregular paleokarst geometries beyond the 2D outcrops. DOMs are obtained through combining a series of overlapping photographs with structure-from-motion photogrammetry, to create mm- to dm-resolution georeferenced DOMs. GPR is typically used for surveying the shallow subsurface and relies on detecting the contrasts in electro-magnetic permittivity. We defined three geophysical facies based on their appearance in GPR. By integrating subsurface geophysical data with DOMs we were able to correlate reflection patterns in GPR with outcrop features. The chaotic nature of paleokarst breccias is seen both in outcrop and GPR. Key horizons in outcrop and the GPR profiles allow tying together observations between these methods. Furthermore, we show that this technique expands the two-dimensional outcrop surface into a three-dimensional domain, thus complementing, strengthening and extending outcrop interpretations.

1. Introduction

Analyzing outcrops is a fundamental technique in many contemporary geological investigations. Digitalization of outcrops, in particular, complements conventional outcrop analysis, allowing for quantitative digital assessment. Digital outcrop models (DOMs) represent a georeferenced 3D view of an outcrop with mm-to dm-scale. DOMs can, therefore, incorporate topographical data of various scales, bridging the gap between centimeter-scale local observations and hundreds of meters-scale seismic structures (Enge et al., 2007). DOMs are becoming a popular tool in geosciences and their advancement over the past two decades has been significant (Buckley et al., 2008, 2019; Carrivick et al., 2016; Enge et al., 2007; Senger et al., 2020; Wilkinson et al., 2016). In the past, high-resolution DOMs were commonly generated using terrestrial or helicopter-mounted light detection and ranging (LIDAR) scanning (Bellian et al., 2005; Buckley et al., 2010; Rittersbacher et al., 2014). However, the expensive nature of the equipment and acquisition and lengthy processing procedures, limited its widespread adoption in

academia. More recently, the rapid evolution of structure-from-motion (SfM) algorithms and their implementation in user-friendly software, has led to an explosion of digital models from a wide variety of sources (Bemis et al., 2014; Carrivick et al., 2016; James et al., 2019; Smith et al., 2016; Westoby et al., 2012). In summary, the increased availability of cost-effective consumer-grade drones with a built-in Global Positioning System (GPS) and high-quality cameras provides a new and potentially game-changing tool for geoscientists (Bemis et al., 2014; Nesbit et al., 2018). Additionally, DOMs are becoming increasingly valuable for teaching and planning geological field campaigns (McCafrey et al., 2010; Senger et al., 2020).

Another widely used technique for shallow subsurface investigations on land is ground penetrating radar (GPR). GPR allows geoscientists to acquire up to cm-scale 2D or 3D geological models of the subsurface (Asprion and Aigner, 1999; Huggenberger, 1993; Kostic and Aigner, 2007). GPR is commonly used to map modern karst caves and paleokarst breccias, allowing the detailed study of their internal and external structures (Chalikakis et al., 2011; Chamberlain et al., 2000; McMechan

* Corresponding author. Department of Arctic Geology, The University Centre in Svalbard, PO Box 156, 9171 Longyearbyen, Norway.

E-mail addresses: janocha@uni-potsdam.de, julian.janocha@web.de (J. Janocha), Thomas.birchall@unis.no (T. Birchall).

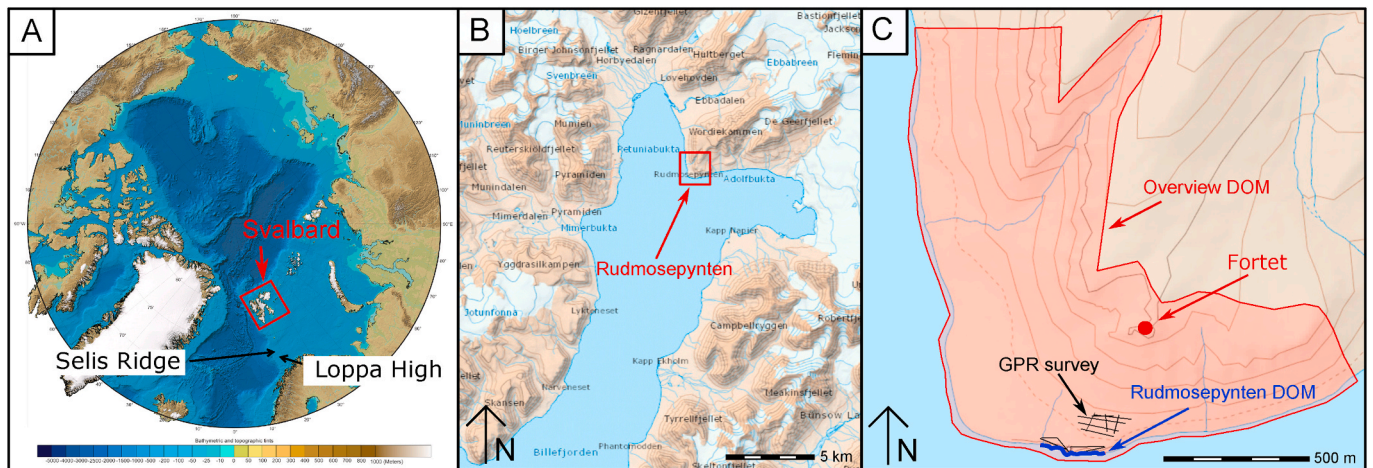


Fig. 1. Geographical location of the study area. **A:** Circum-Arctic bathymetry map showing Svalbard (red box), the Loppa High with the Gotha and Alta discoveries and the Selis Ridge exploration well. Modified from Jakobsson et al. (2012). **B:** Topographical map of Billefjorden with the location of the study area at Rudmosepynten. Map from Norwegian Polar Institute (2014). **C:** Map of the study area. Marked in red are the overview and the Rudmosepynten DOM. Highlighted in black are the profiles of the GPR survey. Map modified from: Norwegian Polar Institute (2014). (For interpretation of the references to color in this figure legend, the reader is referred to the Web version of this article.)

et al., 1998). GPR, along with other ground-based geophysical methods, are tools that meet the challenges originating from lateral and vertical changes of the physical and lithological properties of karst environments, quaternary coastal deposits and coastal barriers (Chalikakis et al., 2011; Jol et al., 1996; Neal et al., 2002).

The integration of GPR with outcrop data enables geoscientists to extend 2D outcrops from the rockface to a third spatial dimension. Despite the advantage of modeling 3D subsurface geometries derived from a GPR grid, this has rarely been performed. Limited case studies have been published on tidal channels, turbiditic sequences and river bar deposits (Bubeck et al., 2011; Jones et al., 2011; Korus et al., 2020; Lee et al., 2007; Pringle et al., 2003, 2006; Wheeler et al., 2011; Young et al., 2003). Luthi and Flint (2014) and Pierce et al. (2018) used shallow borehole data from behind outcrops to extend the knowledge of reservoir architecture but are spatially limited to the well location. Jones et al. (2011), Fernandes et al. (2015); Martinez et al. (1998); Wheeler et al. (2011) and Young et al. (2003) have shown that GPR can be used to extend outcrop analysis into the nearby subsurface. Studies have utilized geophysical techniques to analyze paleokarsts (e.g. Chalikakis et al., 2011; Wheeler et al., 2011), but they have not been directly tied to outcrop.

Paleokarst is a term applied to karst deposits that have been disconnected from the active hydraulic system at some point in time and have been buried by younger rocks. Paleokarst systems are a typical feature in sedimentary basins and in particular in rift basins that comprise evaporitic sequences (Anderson et al., 1978; Blatnik et al., 2020; Blount and Moore, Jr., 1969; Friedman, 1997; Klimchouk et al., 1996; Sayago et al., 2012; Swennen et al., 1990; Tian et al., 2019; Zeng et al., 2011). Here, paleokarst systems mainly develop along faults, fracture networks and bedding planes, showing that active faulting promotes dissolution and subsequent collapse (Palmer, 1991). Paleokarst deposits are strongly heterogeneous and complex with regards to rock texture, structure and pore networks (e.g. Loucks, 1999; Loucks and Mescher, 2001) and are reservoirs in petroleum systems.

The Upper Paleozoic Billefjorden Trough in Svalbard is an example of a rift basin containing thick evaporite sequences and associated paleokarst collapse breccia (Eliassen and Talbot, 2005). The paleokarst system of the Billefjorden Trough is considered as an outcrop analogue to prolific paleokarst plays in the Barents Sea (Eliassen and Talbot, 2005;

Sayago et al., 2012; Solbakk 2020). Both the Gotha (well 7120/1–3) and the Alta (well 7220/11–1) oil discoveries in the Loppa High on the Barents Shelf south of Svalbard are in karstified carbonates of Late Paleozoic age (Matapour et al., 2019), and one recent exploration well on the Selis Ridge (well 7221/4–1) targeted these karstified carbonates (Fig. 1A; “NPD FactMaps Desktop”, 2020; Solbakk, 2020). Therefore, investigations of the paleokarst system of the Billefjorden Trough may play a role in mitigating risk related to exploration on the Barents Shelf and similar basins.

In this case study we investigate the Billefjorden Trough paleokarst system at Rudmosepynten in inner Billefjorden, Svalbard (Fig. 1B,C), by combining a GPR dataset with a DOM and conventional geological data from an extensive paleokarst outcrop near the Fortet locality. In addition, we propose a workflow for DOM and GPR processing, as well as the integration of outcrop data with DOMs and GPR. This approach enables us to link sedimentary facies observed in the outcrop to GPR facies.

2. Geological setting

In central Spitsbergen, the north-south striking Billefjorden Trough consist of up to 2000 m thick, westward thickening, mixed syn-rift successions of siliciclastics, evaporites and carbonates (Braathen et al., 2011; Harland et al., 1997; Johannessen and Steel, 1992; Smyrak-Sikora et al., 2019). These units were deposited in arid to semi-arid climate conditions in Carboniferous times (Late Serpukhovian-Moscovian) (Cutbill and Challinor, 1965; Holliday and Cutbill, 1972; Johannessen and Steel, 1992). The overlying post-rift succession of Late Carboniferous-Permian age consists of up to 100 m thick interbedded carbonate and evaporite-platform deposits that cover most of central Spitsbergen (Sorento et al., 2020).

The Billefjorden Trough formed on the hanging wall of the Billefjorden Fault Zone (BFZ) - a crustal-scale boundary between Devonian sedimentary units to the west and metamorphic pre-Caledonian basement to the east (Braathen et al., 2011; Harland et al., 1997). During the Carboniferous, the BFZ reactivated as a normal fault in response to regional extension (Faleide et al., 1984; Harland et al., 1974). The Carboniferous deformation comprises a set of syn-depositional faults formed along the hanging wall block, antithetic to the BFZ (Braathen

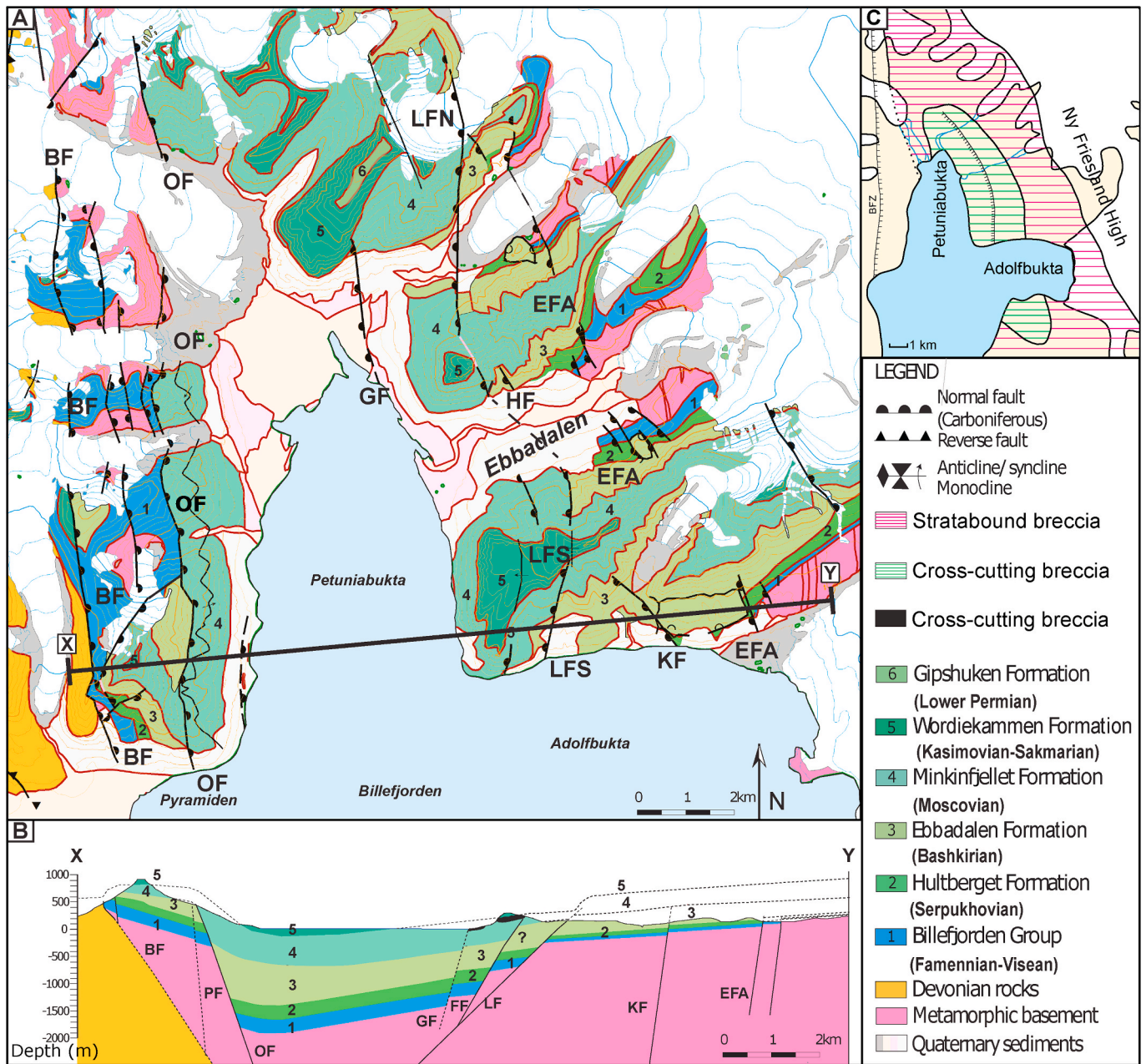


Fig. 2. Geological overview of inner Billefjorden. **A:** Geological map of inner Billefjorden. Showing the Upper Paleozoic Billefjorden Trough succession and the basin bounding faults in the east and west. **B:** Geologic cross-section from west to east. Transect through the asymmetric Billefjorden Trough. Showing the basement and the Upper Paleozoic Billefjorden Trough succession, including the carbonate breccias of the Fortet Member. BF: Balliolbreen Fault; EFA: Ebbabreen Fault Array; FF: Fortet Fault; GF: Gizehfjellet Fault; HF: Hultberget Fault; KF: Kampesteindalen Fault; LF: Løvehovden Fault; LFN: Løvehovden Fault North; LFS: Løvehovden Fault South; OF: Odellfjellet Fault; PF: Pyramiden Fault. **C:** Map of cross-cutting (green striped) and stratabound (red striped) paleokarst breccias. Map modified from Eliassen and Talbot (2005). (For interpretation of the references to color in this figure legend, the reader is referred to the Web version of this article.)

et al., 2011; Maher and Braathen, 2011; Smyrak-Sikora et al., 2019). Minor, post-rift fault activity along the BFZ persisted into the Permian (Ahlborn and Stemmerik, 2015; Maher and Braathen, 2011; Stemmerik and Worsley, 2005). In the Paleogene, during the Eurekan transpressional tectonic event, several of these faults were reactivated as reverse faults (Bælum and Braathen, 2012; Bergh et al., 2000; Braathen et al., 1999; Haremo et al., 1990; Manby et al., 1994; McCann and Dallmann, 1996).

The deposition of the syn-rift strata within the Billefjorden Trough initiated in Serpukhovian with the accumulation of siliciclastic red beds of the Hultberget Formation, interpreted as terrestrial fluvial and overbank deposits (Johannessen and Steel, 1992). The Bashkirian aged

Ebbadalen Formation is interpreted as being paralic, with units consisting of terrestrial to shallow marine siliciclastic deposits, gypsum beds formed in sabkhas and salinas, and restricted to open marine carbonates deposited and intercalated with black shales (Holliday and Cutbill, 1972; Johannessen and Steel, 1992; Smyrak-Sikora, 2020; Smyrak-Sikora et al., 2019).

The Minkinjfellet Formation (Fig. 2) comprises up to 500-m-thick beds of gypsum and carbonates with subsidiary sandstone layers (Eliassen and Talbot, 2003b; Smyrak-Sikora, 2020; Verba, 2013). The unit was deposited in a shallow, tidally influenced marine basin environment, overlapping the Ny Friesland High to the east (Dallmann, 1993; Eliassen and Talbot, 2003b; Lønøy, 1995). The overlying syn- to post-rift

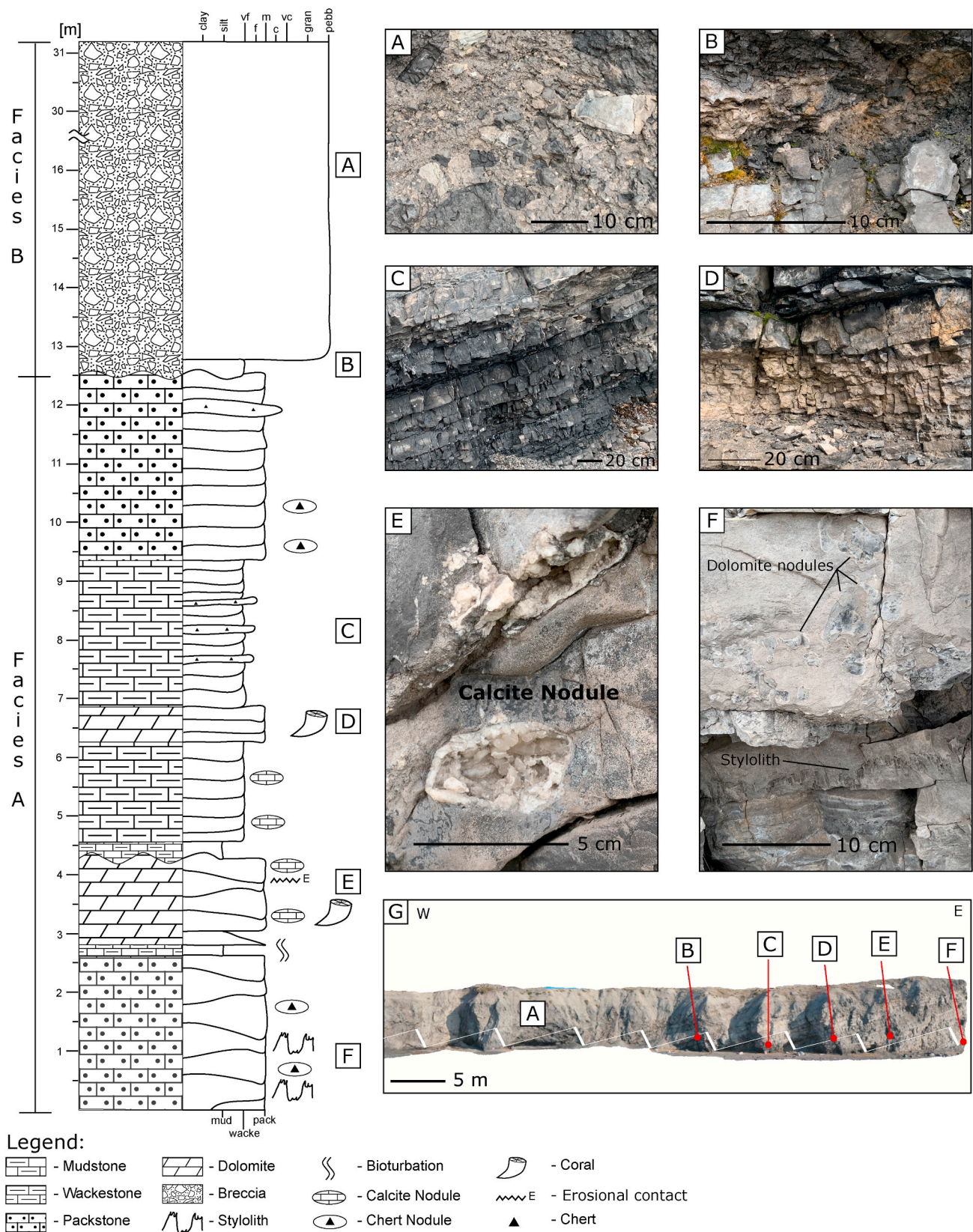


Fig. 3. Stratigraphic log through the Minkinfjellet carbonates and the paleokarst breccias at Rudmosepynten. **A:** Paleokarst breccia, lithofacies B. **B:** Clay layer at the base of the paleokarst breccias, lithofacies B. **C:** Section of wackestone and chert beds in lithofacies A. **D:** Dolomitic section in lithofacies A. **E:** Calcite nodule in dolomitic section of lithofacies A. **F:** Dolomite nodules and styloliths in packstone section of lithofacies A. **G:** Image of the outcrop showing the locations of the images. The trace of the stratigraphic log is highlighted by the thick sections of the white line. (For interpretation of the references to color in this figure legend, the reader is referred to the Web version of this article.)

Table 1
Acquisition parameters for the photogrammetric and GPR survey.

Photogrammetry parameters		Ground penetrating radar parameters	
Acquisition type	Drone	Antenna configuration	In-line parallel
Type model	DJI Mavic 2 Pro	Transmitter Receiver offset	2 m
Camera	Built-in 20 Megapixel	Antenna centre frequency	50 MHz
Georeferencing	Ground calibration points (eTrex 10 GPS)/Built-in GPS module of the drone	Transmission trigger mechanism	Time triggered
Recording format	Video	Time interval	0.01 s
Recording parameters	1920 x 1080 @30 fps	Recording time window	850 ns

Wordiekammen Formation is a carbonate dominated succession that extends regionally over the flanks of the Billefjorden Trough (Braathen et al., 2011; Dallmann, 1999; Pickard et al., 1996). These formations commonly display oil staining and exhibit a strong hydrocarbon odor, presumably generated from the organic-rich lagoonal carbonate mudstones which were deeply buried until the past few Myr (Henriksen et al., 2011a; Nicolaisen et al., 2019).

The Fortet Member, the focus of this study, is a locally developed member of the Minkinfjellet Formation and consists of carbonate breccia, formed by karstification of the carbonate-evaporite succession

Table 2
DOM specific parameters. Modified from Janocha (2020).

Model	Original number of images	Number of processed images	Ground resolution	Distance to outcrop	Covered area
Rudmosepynten	1 222	458	0.7 cm/pix	17.3 m	2 310 m ²
Overview	124	124	14.6 cm/pix	621 m	587 000 m ²
South Central	949	415	1.3 cm/pix	35.6 m	4 440 m ²
South East	2 053	898	1.2 cm/pix	35.6 m	5 990 m ²
East	88	88	1.2 cm/pix	26.8 m	664 m ²
Block East	99	99	0.9 cm/pix	18.8 m	351 m ²
North	1 141	645	1.5 cm/pix	46.8 m	5 880 m ²
Pinnacle	922	445	1.8 cm/pix	54.3 m	293 m ²
Block West	185	185	1.7 cm/pix	53.3 m	549 m ²
Caves	983	485	0.7 cm/pix	19.2 m	2 010 m ²
Gypsum breccia	262	262	1.1 cm/pix	67.6 m	6 660 m ²

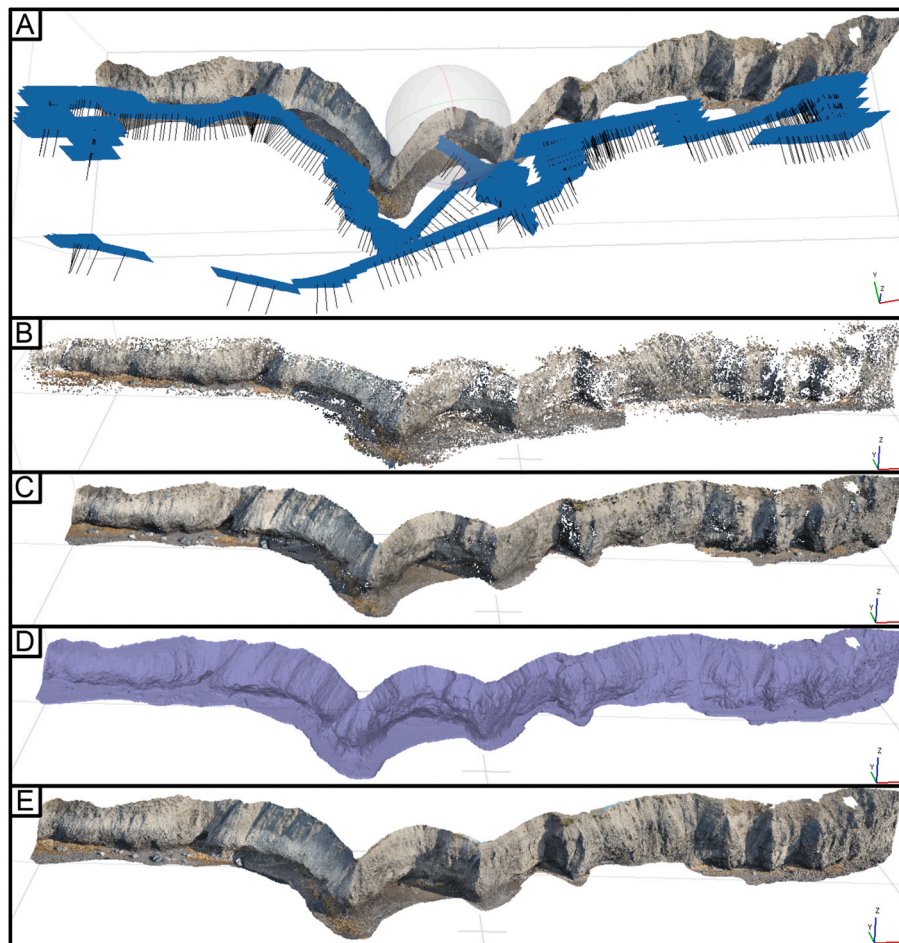


Fig. 4. From outcrop to digital outcrop model: Processing steps. A: Aligning photos. B: Sparse cloud. C: Dense cloud. D: Mesh of triangulated surfaces. E: Textured layer from pictures draped on mesh. (For interpretation of the references to color in this figure legend, the reader is referred to the Web version of this article.)



Fig. 5. GPR survey profile locations. **A:** Overview DOM showing the Talus slope and locations of key GPR profiles 2 and 12. **B:** Map of Rudmosepynten showing the locations of the GPR profiles 1–13 used for the integration and interpretation in this paper. Map from: [Norwegian Polar Institute \(2014\)](#). (For interpretation of the references to color in this figure legend, the reader is referred to the Web version of this article.)

of the Minkinfjellet Formation and upper part of Ebbadalen Formation (Fig. 2B). This occurred due to the dissolution of gypsum beds (Eliassen and Talbot, 2003b; Lønøy, 1995). Two types of paleokarst breccia have previously been recognized: (i) vertical cross-cutting bodies (pipes) (Fig. 2C) located along faults (i.e. Løvehovden Fault Zone) were interpreted to have formed in the Early Permian, during a post-rift phase of the Billefjorden Trough (Eliassen and Talbot, 2003b, 2005); (ii) horizontal strata-bounded breccias (Fig. 2C) (Eliassen and Talbot, 2003b, 2005) located along the flanks of the Billefjorden Trough formed during the Late Carboniferous, due to syn-depositional uplift along fault blocks (Smyrak-Sikora, 2020). Eliassen and Talbot (2003a) suggest that the dissolution and brecciation observed within the Minkinfjellet Formation

is related to periods of subaerial exposure occurring contemporaneously with the deposition of the overlying Wordiekammen Formation (Fig. 2). Evidence for continuous deformation during and after the deposition of the paleokarst breccias occur as faults in the breccias of the Fortet outcrop (Janocha, 2020).

3. Methods and data

3.1. Lithofacies

All the associated data presented in this study are collected from the Rudmosepynten outcrop area near the Fortet locality in the innermost

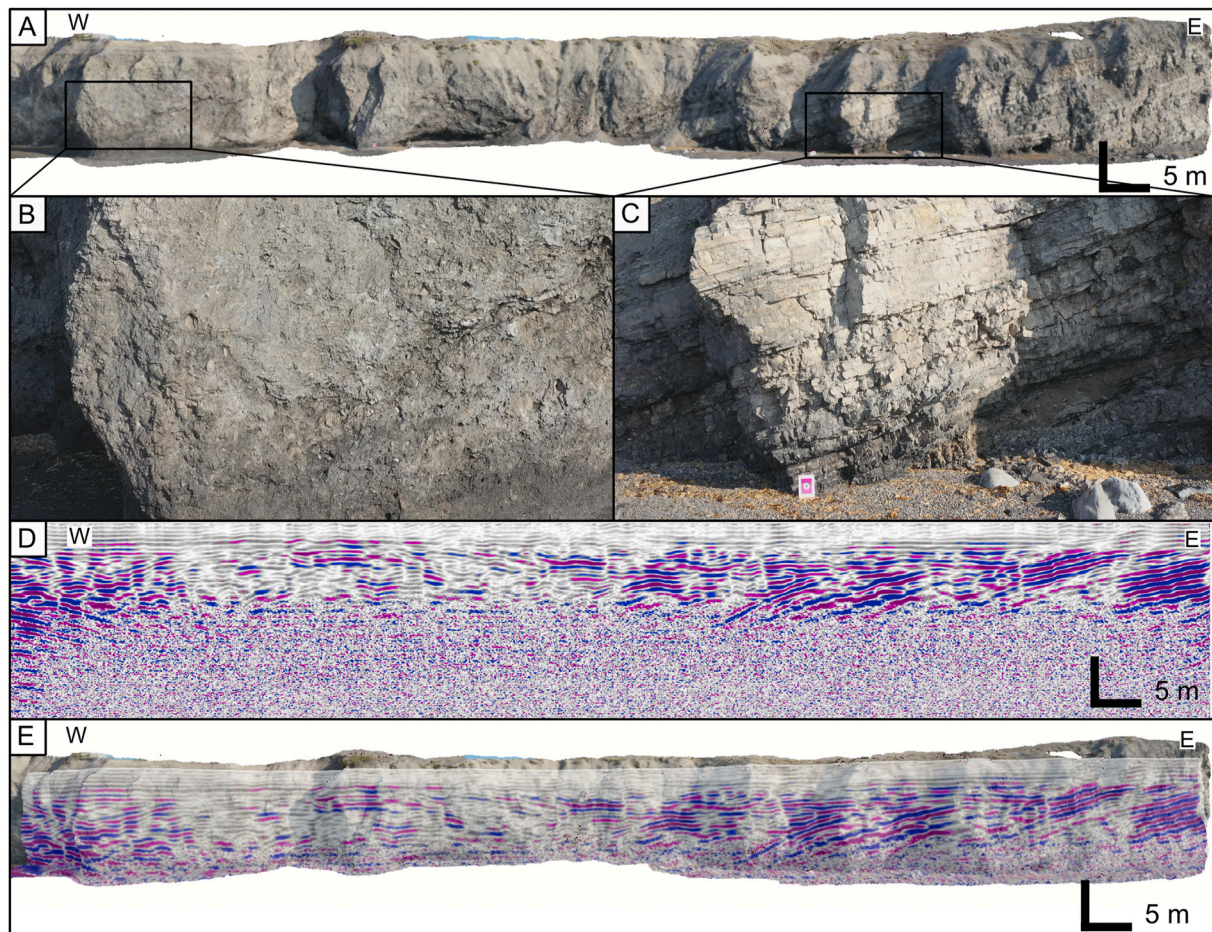


Fig. 6. Draping GPR profile 2 over the Rudmosepynten DOM. **A:** DOM of the outcrop. Showing the eastern most section of the DOM. **B:** closeup on the paleokarst breccias of lithofacies B. **C:** Closeup on the dipping carbonate layers of lithofacies A. **D:** GPR profile 2 acquired 3 m behind and parallel to the outcrop. **E:** Data integration by draping the GPR profile on the model in LIME. (For interpretation of the references to color in this figure legend, the reader is referred to the Web version of this article.)

part of Billefjorden (Fig. 1B,C). This is the type locality for the Fortet Member, in which the investigated breccias occur. The Rudmosepynten outcrop stretches in east-west direction over 300 m along the coastline at Rudmosepynten. With a height of approximately 10 m it forms a cross-section through the adjacent plateau. Detailed stratigraphic logging and sedimentological descriptions are used to describe the outcrop and define lithofacies. A 30 m long sedimentological log in 1:50 scale was collected along the Rudmosepynten outcrop that represent lithofacies A and B (Fig. 3).

3.2. Digital outcrop models (DOMs)

The photogrammetric models are based on videos from a GPS-enabled drone (Table 1). To ensure sufficient image overlap, the drone was flown at a constant speed (5 m/s) along the outcrop while recording video. Every 15th frame was extracted from each video using Agisoft Metashape Professional software (Agisoft, 2020). For georeferencing the Rudmosepynten DOM, four ground control points were placed along the outcrop and their position was determined with a Garmin eTrex 10 GPS in averaging mode (uncertainty ± 1 m). The overview DOM was georeferenced using images georeferenced by the drones built-in GPS. The images were processed into a DOM using proprietary algorithms in Agisoft Metashape (Fig. 4). For efficient processing, extracted frames were pre-selected using a MATLAB script with those having >90% overlap removed. Processing includes the alignment (Fig. 4A) of the pictures with fixed camera positions where overlapping photos are

aligned by a selection of points to create a sparse point cloud (Fig. 4B). The next step was to expand the point cloud into a dense cloud (Fig. 4C) from which a wireframe mesh of triangulated surfaces was generated (Fig. 4D). A texture layer generated from images was added to the mesh (Fig. 4E). The DOM was exported as a *.obj file georeferenced in UTM coordinates for use with interpretation software. We acquired and processed 11 DOMs from the area surrounding Fortet (Table 2; Janocha (2020); supplementary material). In this contribution we present an overview DOM (Fig. 5A) and a detailed DOM of the Rudmosepynten outcrop (Fig. 6A). The overview DOM covers an area of 587,000 m², with a pixel resolution of 14.6 cm/pixel. The Rudmosepynten outcrop DOM, covers an area of 2310 m² with a pixel resolution of 0.7 cm/pixel (Fig. 6A).

A supplementary video summarizing the article with additional Figures and visual explanations can be found at <https://doi.org/10.1016/j.marpetgeo.2020.104833>

3.3. Ground penetrating radar (GPR)

The GPR survey was acquired using a 50 MHz MÅLA Rough Terrain Antenna (Table 1). Each trace of the GPR profiles was georeferenced with a Garmin eTrex 10 GPS connected to the MÅLA CV monitor. The antennas emit electromagnetic waves in the range of 10s to 100s of MHz. The vertical resolution in GPR is fully dependent on the emitted wavelength in the subsurface (Equation (1)). These waves are then reflected by contrasts in electro-magnetic permittivity in the subsurface. GPR

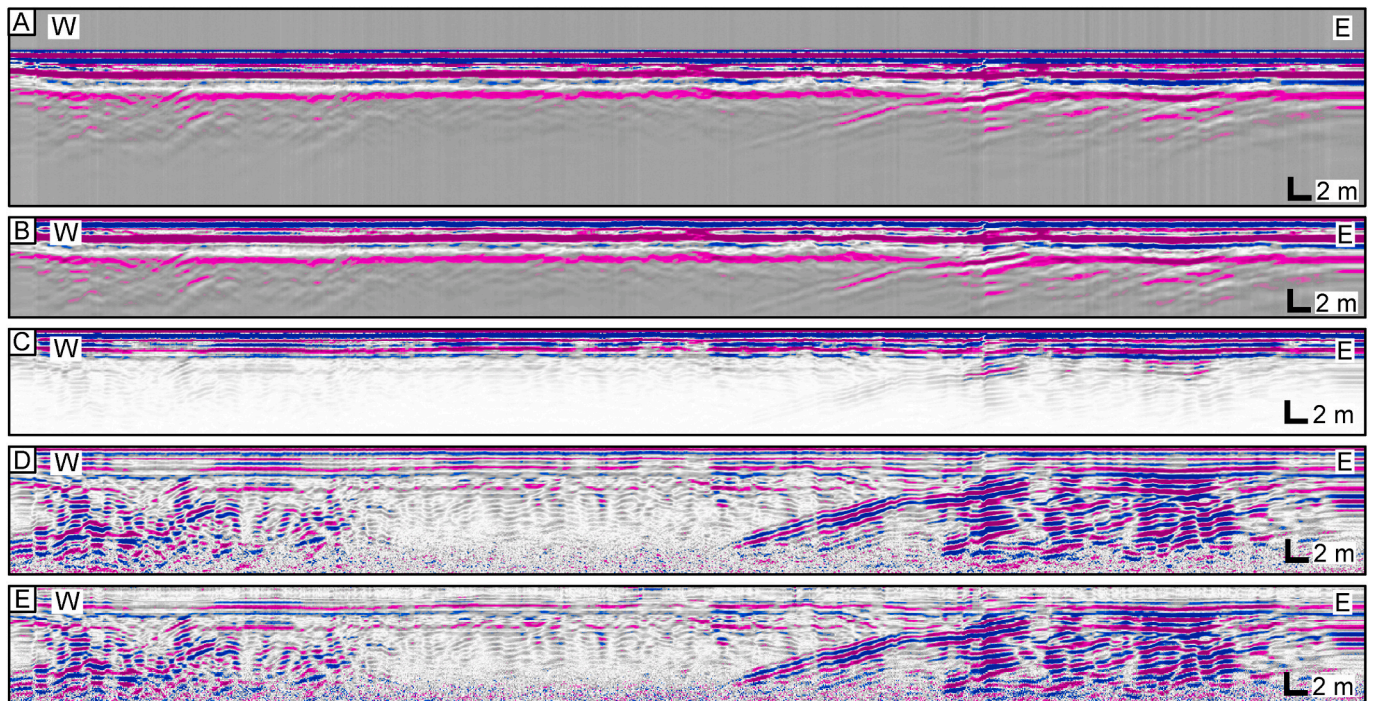


Fig. 7. Processing steps of GPR data in ReflexW following Senger et al. (2014). Exemplified on GPR profile 6. **A:** Time-depth conversion. Transformation of two-way-travel time on the y-axis to depth using 0.12 m/ns as a constant electro-magnetic wave speed based on values from Robinson et al. (2013). **B:** Move start time correction. **C:** Dewow filtering. **D:** Energy decay function accounting for attenuation with depth. **E:** Background removal reducing the airwave. (For interpretation of the references to color in this figure legend, the reader is referred to the Web version of this article.)

acquisition was carried out in April 2018 on snow covered ground. The snow cover and frozen active permafrost layer allowed fast acquisition with no environmental impact on the vegetation and soil. To account for the offset between the GPS and the GPR antennas, a MATLAB script corrected the location of every GPR trace regarding this offset. Processing of data was performed using the ReflexW (software) (Sandmeier, 2019) following the processing steps in Senger et al. (2014), who investigated structural heterogeneity in Jurassic sandstones in Svalbard, using the same equipment. The basic processing involved moving the first arrival to the top of the profile (Fig. 7B), dewow filtering (Fig. 7C), accounting for attenuation by applying an energy decay function (Fig. 7D). Furthermore, the airwave was reduced by a background removal (Fig. 7E). A time-depth conversion (Fig. 7A) with a constant velocity of 0.12 m/ns (Robinson et al., 2013) was used to display the y-axis as depth instead of two-way-travel time.

$$\text{vertical resolution} = \frac{\text{wavelength}}{4} \quad (1)$$

In this contribution, we focus on 13 GPR profiles with a total length of 1.4 km. These GPR profiles were acquired directly on top of the Rudmosepynten outcrop, including 9 profiles striking outcrop-parallel and 4 outcrop-perpendicular (Fig. 5B). GPR profile 2 (Fig. 6B) represents an outcrop-parallel profile acquired approximately 3 m behind the outcrop, whereas GPR profile 12 represents an outcrop-perpendicular profile acquired towards a talus slope (Fig. 5B).

3.4. Data integration

Integration of the DOM and GPR survey was carried out in the LIME virtual outcrop interpretation software, version 2.1.9.1 (Buckley et al., 2019). These interpretations are based on visual observations and limited by mesh resolution and DOM resolution. Fig. 8 visualizes the steps from image and GPR acquisition, DOM and GPR processing to DOM and GPR integration. To load the DOMs into the interpretation software the DOM is required to be in UTM coordinates. The GPR

profiles were imported to LIME as image panels. These panels were manually placed within the working environment using the start and end coordinates of the GPR profile.

4. Results and interpretation

4.1. Facies description and interpretation

The different facies types described from outcrop and DOM observations are lithofacies A, B and C, in the GPR profiles GPR facies A, B and C are observed. Lithofacies B and GPR facies B are overlying and younger than lithofacies A and GPR facies A.

4.1.1. Facies A

Description of lithofacies A: In outcrop lithofacies A consists of inter-bedded wackestones, packstones, dolomites and mudstones with clear bedding thickness of 10 cm to 1 m. Lithofacies A is of carbonate composition and has a strong smell of hydrocarbons. The upper part of the outcropping succession is dominated by parallel bedding whereas the lower part exhibits sinusoidal bed geometries. The color of lithofacies A is the same dark grey as the clasts of lithofacies B (Fig. 3C-E and Fig. 9A,B). The interval gently dips to the west with an inclination of 16°. In the DOM lithofacies A is easily identifiable by its characteristic westward titled carbonate benches (Fig. 9A,B). All but the thinnest intervals of lithofacies A are resolvable in the DOM.

Description of GPR facies A: GPR facies A dominates the eastern part of the survey area (Fig. 9C and Fig. 10C,D). It is characterized in the GPR data by stronger, coherent and continuous westward-dipping reflectors. GPR facies A appears to sharply underlie GPR facies B. GPR facies A shows slightly deeper (0.5 m) GPR penetration than GPR facies B.

Interpretation of Facies A: Lithofacies A is interpreted to represent carbonate benches of the Minkinfjellet Formation. Strata of this lithology is also the likely source of carbonate wackestone and packstone clasts that dominate the paleokarst breccia of lithofacies B. Lithofacies A was deposited in a shallow marine, tidally influenced basin and was

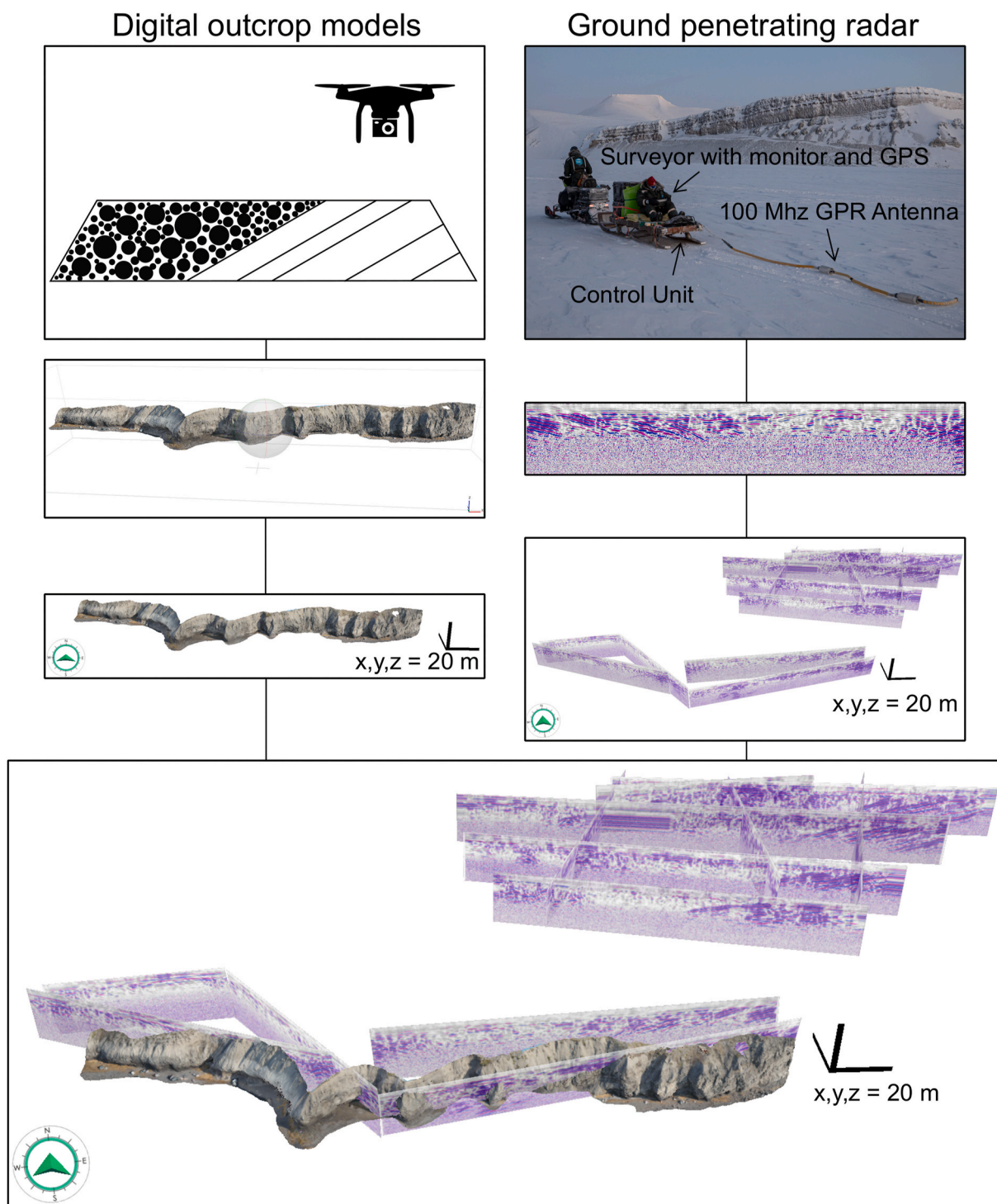


Fig. 8. From data acquisition to data integration. Flowchart showing the stages of acquisition, processing, LIME import and data integration in a fully georeferenced 3D environment. (For interpretation of the references to color in this figure legend, the reader is referred to the Web version of this article.)

deposited prior to lithofacies B (Eliassen and Talbot, 2003b). The contact of lithofacies A to lithofacies B is interpreted as the base of the paleo-cave system. In the GPR profiles the contact between GPR facies B and GPR facies A is marked by a sharp boundary. This boundary is dip parallel to the dipping reflectors of GPR facies A. This prominent reflector correlates well with measurements of the outcrop contact which makes it an ideal candidate to analyze the distribution and geometry of the paleo-karst system in the GPR data.

4.1.2. Facies B

Description of lithofacies B: Lithofacies B exclusively dominates the western section of the outcrop. In outcrop, lithofacies B appears as a chaotic clast-supported conglomerate. No obvious depositional structures were observed with regards to clast distribution or the matrix. The conglomerate consists of (very poorly sorted) micritic (sub-rounded to sub-angular) clasts and are 2–10 cm large (Fig. 3A and Fig. 9D,E). The matrix is composed of clay grade material of dark grey coloration. Both the clasts and matrix have a carbonate composition. The transition from lithofacies A to the overlying lithofacies B is marked by a sharp dip

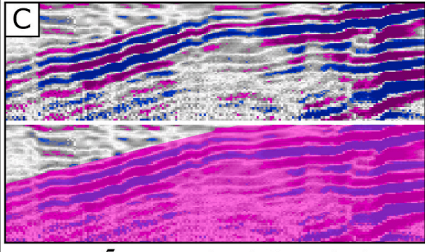
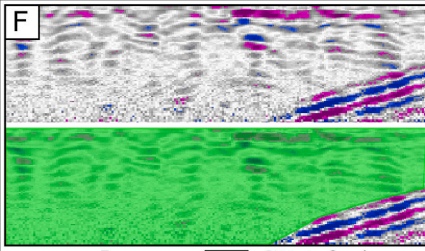
	Outcrop	Digital Outcrop Model	Ground Penetrating Radar
Facies A			
	Observations		
	<ul style="list-style-type: none"> - Composition: Micritic Limestone - Bed thickness: 2-100 cm - Bedding: 278/16 	<ul style="list-style-type: none"> - Tilted beds - Bed thickness: 10-100 cm - Outcrop length: 50 m - Bedding: 269/17 	<ul style="list-style-type: none"> - Reflectors: coherent & strong - Tilted westward - Location: restricted to the east - Dip parallel boundary to Facies B - Tilt: 275/19
	Interpretations		
<ul style="list-style-type: none"> - Minkinfjellet Formation Limestones - Paleo-cave floor 	<ul style="list-style-type: none"> - Minkinfjellet Formation Limestone - Paleo-cave floor 	<ul style="list-style-type: none"> - Host rock lithology - Paleo-cave floor 	
Facies B			
	Observations		
	<ul style="list-style-type: none"> - Lithology: Breccia - Clast size: 2-10 cm - Composition: micritic limestone - Roundness: sub-rounded/angular - Matrix composition: carbonated 	<ul style="list-style-type: none"> - Lithology: Breccia - Clast size: 5-10 cm - Outcrop length: 150 m - Outcrop height: 12 m 	<ul style="list-style-type: none"> - Reflectors: weak - Signal characteristic: diffracted - Location: restricted to the west
	Interpretations		
<ul style="list-style-type: none"> - Paleokarst breccia - Paleo-cave sedimentary fill 	<ul style="list-style-type: none"> - Breccia 	<ul style="list-style-type: none"> - Breccia 	

Fig. 9. Description and interpretation of facies A and B. Comparison of observations made on facies A and B in the field, the DOM and GPR. A: Outcrop picture of lithofacies A. B: Exported image of lithofacies A from DOM. C: Section of GPR facies A in GPR profile 2. D: Outcrop picture of lithofacies B. E: Exported image of lithofacies B from DOM. F: Section of GPR facies B in GPR profile 2. Orientations are presented in azimuth/dip angle convention throughout the figure. (For interpretation of the references to color in this figure legend, the reader is referred to the Web version of this article.)

parallel boundary. Directly at the contact to lithofacies A this facies has a thin (10 cm) clay layer (Fig. 3B). In the DOM, lithofacies B is identifiable by the lack of stratification. Some smaller clasts are indistinguishable in the DOM despite a resolution of 0.7 cm/pixel due to the similarity in clast color and appearance.

Description of GPR facies B: GPR facies B is prominent in the GPR profiles and dominates the western parts of the survey area (Fig. 9F and Fig. 10C,D). It is characterized by discontinuous and often chaotic reflectors. GPR facies B typically shows a dimming response in comparison to the surrounding intervals. The transition from GPR facies B into GPR facies A is typically abrupt and coherent.

Interpretation of facies B: The conglomeratic composition of facies B and its sharp boundary to facies A (as described above) is interpreted as a dissolution collapse breccia (Friedman, 1997; Klimchouk et al., 1996; Loucks, 1999). Gypsum clasts are observed in the Fortet Member in other parts of the basin so is almost certainly the dissolved mineral responsible for brecciation (Eliassen and Talbot, 2005). The local geology and overview DOM also suggest that this facies is a component of a larger karst system that has been subsequently buried; therefore, facies B is classified as a paleokarst breccia. Paleo-cave roof collapse and clast transportation within the paleo-cave resulted in the deposition of a breccia with sub-rounded clasts.

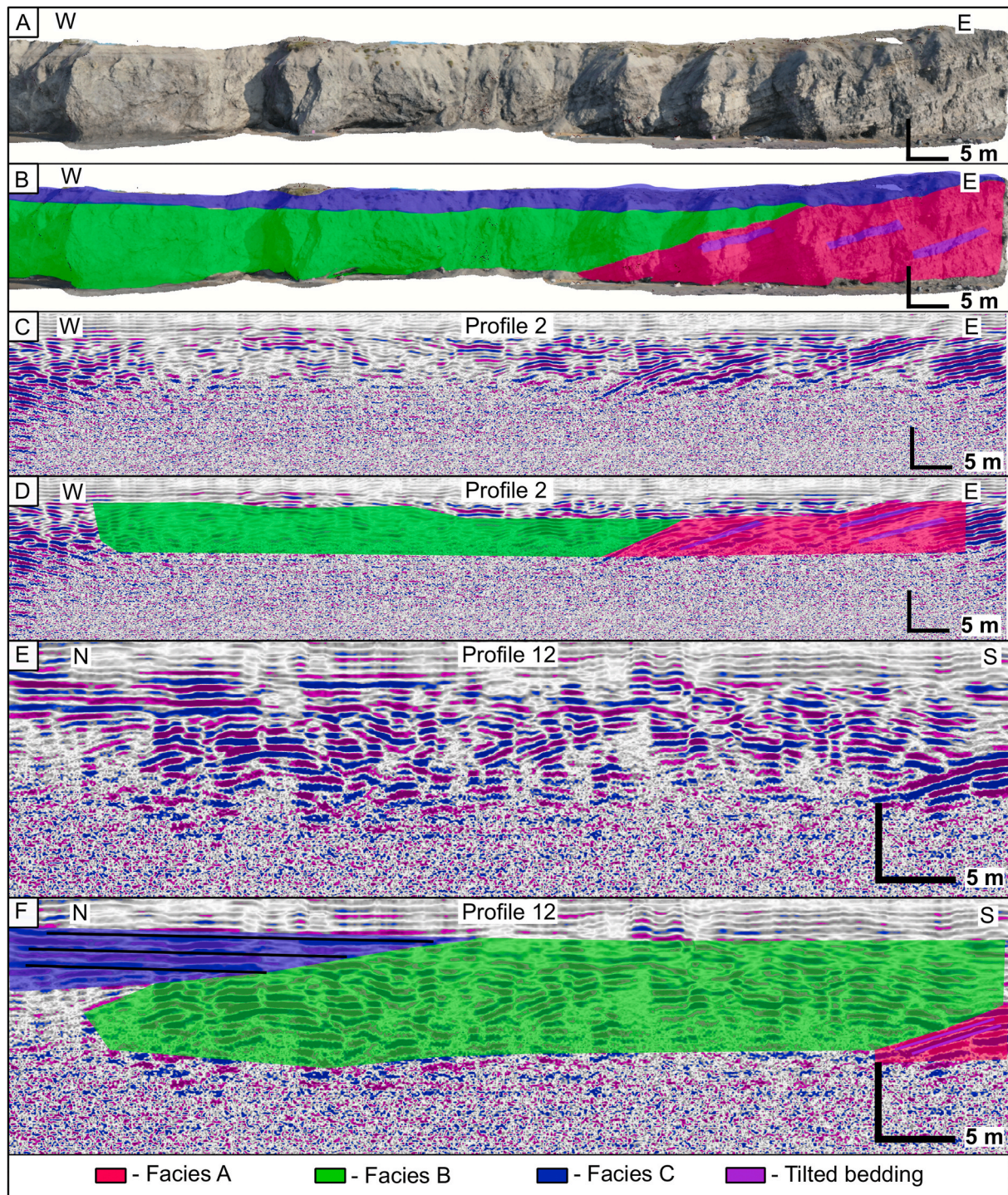


Fig. 10. DOM and GPR interpretations. GPR profile 2 and the DOM are interpreted at the same scale and show the same section. GPR profile 12 is perpendicular to the outcrop and acquired in the northern section of the survey area. **A:** Uninterpreted orthographic image of the eastern most section of the DOM. **B:** Geologic interpretation of the outcrop draped on the DOM. lithofacies B dominating the western section whereas lithofacies A is dominating the eastern section. **C:** Processed GPR profile 2. **D:** GPR profile 2 interpreted exhibiting GPR facies B in the western section and GPR facies A in the eastern section. The boundary between GPR facies A and B is sharp and dip parallel. **E:** Processed GPR profile 12. **F:** Interpretation of profile 12. The central part of the profile is dominated by GPR facies B. Towards the south GPR facies A is present whereas the northern end of the profile is characterized by GPR facies C. (For interpretation of the references to color in this figure legend, the reader is referred to the Web version of this article.)

4.1.3. Facies C

Description of lithofacies C: Lithofacies C is observed in a 50 cm thick exposure in the upper most part of the outcrop. Lithofacies C is formed by loose unsorted sediment of light grey color and appears to show horizontal stratification (Fig. 10A,B). Lithofacies C forms a scree that

covers the lithified part of the outcrop.

Description of GPR facies C: GPR facies C is only recognized in the northern end of the outcrop perpendicular profiles. Its reflectors contrast clear to the geophysical character of GPR facies B and GPR facies A. GPR facies C displays horizontal, continuous reflectors. The abrupt

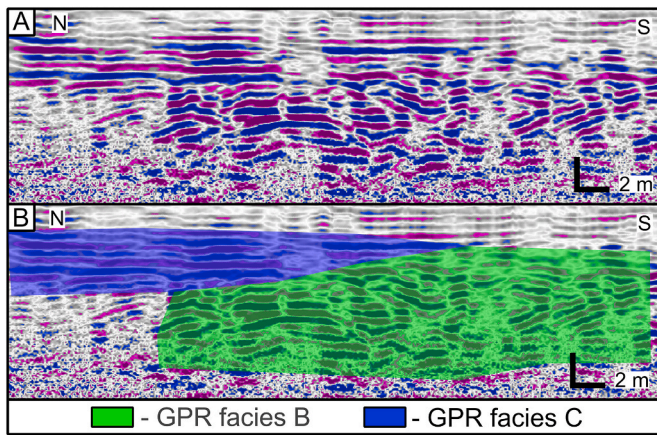


Fig. 11. Northern section of GPR profile 12. **A:** Processed GPR profile 12. **B:** Interpreted image of the same section. Facies C is marked in blue with black lines highlighting the horizontal reflectors. These contact to facies B is interpreted as sedimentary onlap towards the south. (For interpretation of the references to color in this figure legend, the reader is referred to the Web version of this article.)

termination of these horizontal reflectors against the chaotic GPR facies B indicates an onlapping relationship (Fig. 10F and Fig. 11B).

Interpretation of facies C: Lithofacies C and GPR facies C likely represent Quaternary talus slope or beach gravel deposits. Quaternary talus slope deposits as observed in the Fortet overview DOM (Fig. 5, A) are supported from GPR characteristics presented by Onaca et al. (2016) from a similar geological setting. The horizontal reflectors are interpreted to represent modern talus shedding events with periodically intense rockfalls, comprising of poorly sorted detritus of the exposed Wordiekammen Formation. The beach gravel deposits, on the other hand, are supported by episodes of relative sea-level drop due to isostatic rebound (Forman et al., 2004). Beach gravel sediments are often characterized by horizontal to sub-horizontal deposits (Neal et al., 2002; Nemeč and Steel, 1984). The link between lithofacies C and GPR facies C is not straight forward and these two facies might therefore represent two different depositional environments. Both lithofacies C in the outcrop and GPR facies C are interpreted to represent recent, Quaternary un lithified deposits.

5. Discussion

5.1. Dataset integration

The integration of the datasets allows to directly correlate outcrop features to GPR reflectors. GPR profile 2 was acquired 3 m behind the outcrop and therefore portrays nearly the same features as the outcrop (Fig. 10A-D). Furthermore, eastwards from the contact of facies B to facies A, the westward dipping carbonate benches of the Minkinfjellet Formation correlate with the westward dipping GPR reflectors (Fig. 10B, D). Tilted carbonate beds (facies A) have a sharp bedding dip-parallel boundary with the paleokarst breccias (facies B). The orientation of the boundary between facies B and facies A in the outcrop, the DOM and the GPR profiles is expressed consistently in all datasets (Fig. 9). This confirms that the paleo-cave base is observed in the outcrop and GPR survey. In addition, the chaotic paleokarst breccias in the outcrop correlate with chaotic diffracted GPR reflectors. The quaternary colluvial deposits of GPR facies C were not correlated to the outcrop, however, the overview DOM demonstrates that this contact overlaps with a pronounced increase in steepness of the talus slope (Fig. 5A).

5.2. Breccia genesis, extent and geometry

Displaying the interpretations of the GPR profiles together with the

DOMs (Fig. 12B) suggests that facies B dominates the entire survey area. Conversely, facies A is restricted to the eastern areas of the survey site. Typically, the coherent sharp, dip-parallel transition from paleokarst breccias to undisturbed stratigraphy is one of the key characteristics of karst and paleokarst features in evaporitic karst systems, where it marks the paleo-cave floor (Simpson, 1988). In depositional terms, facies B represents the stratigraphic level of gypsum deposition which was later dissolved and replaced by the paleokarst breccias of lithofacies B, whereas the carbonates of facies A are relatively stable (Fig. 13; Eliassen and Talbot, 2005). Higher up in the stratigraphic succession at Wordiekammen, located 2 km to the north-east from the Rudmosepynten outcrop, the Wordiekammen Formation is intersected by cross-cutting paleokarst breccia pipes (Eliassen and Talbot, 2005; Nordeide, 2008; Wheeler et al., 2011). These are displayed as vertical 42.5 m wide and 105.5 m high pipes interpreted in the outcrop (Nordeide, 2008) and are shown as diffracted signals in GPR acquired on Wordiekammen by Wheeler et al. (2011). At Rudmosepynten we are able to show that the paleokarst breccia extends for more than 150 m beyond the outcrop and form a connected paleo-cave system exceeding the area of 16 000 m² (Fig. 12A). This study suggests that the continuous paleo-cave system extends further under Wordiekammen (Fig. 12A) and is likely to be the underlying source determining the presence of the cross-cutting breccia pipes on the Wordiekammen Plateau. This is supported by the occurrence of undissolved gypsum further to the north, in the lateral position of the paleokarst breccias as suggested by Eliassen and Talbot (2005).

This study investigated breccia deposition immediately above the paleo-cave base. Expanding the area of investigation to other parts of the paleokarst succession may help to understand paleokarst depositional environments, irregular geometries and their extent beyond the outcrop.

Dissolution collapse breccias are a targeted hydrocarbon reservoir in other Carboniferous rift sequences on the Barents Shelf (Sayago et al., 2012). By understanding their geometry and scale in Svalbard we can better understand their potential offshore. This approach is not only relevant for paleokarst outcrops and analogues but can also be transferred to other petroleum systems such as karstified carbonates (Fernandes et al., 2015) and other limestone reservoirs (Martinez et al., 1998).

5.3. Method assessment

This study shows that the integration of DOMs with GPR profiles has the potential of directly linking GPR reflection patterns to outcrop equivalents. Ensuring that the GPR is portraying the nearly vertical outcrop, it has to be followed by a surface suitable for GPR acquisition. Moreover, the resolution of the DOM and GPR limit the interpretation and linkage exemplified in the portraying of carbonate beds. All datasets need a surface or feature that can without doubt be correlated across the datasets. The westward dipping carbonate layers of facies A offer a good opportunity to quantify the differences in vertical resolution between each method. In the outcrop we identified more than 60 carbonate beds. In contrast, only a total of 49 carbonate beds can be identified from the DOM. With the relationship of the vertical resolution being one quarter of the GPR wavelength for this study the vertical resolution is 0.6 m, resulting in the imaging of 19 tilted reflectors. This comparison shows that both the DOM and GPR are not able to resolve the details of outcrop in full, thus emphasizing the necessity of obtaining detailed data from conventional fieldwork to compliment and ground truth model interpretations. Future efforts could include vertical radar profiling to compare GPR reflection characteristics with lithology (Pringle et al., 2003).

It is important to stress that both the DOM and GPR datasets rely on a good description of the outcrop. The direct correlation in more complex geological environments also requires good knowledge about subsurface geophysical parameters for a precise illustration of the subsurface. This method allows us to increase the certainty of digital and geophysical interpretations. In a future step the direct correlation of the datasets into

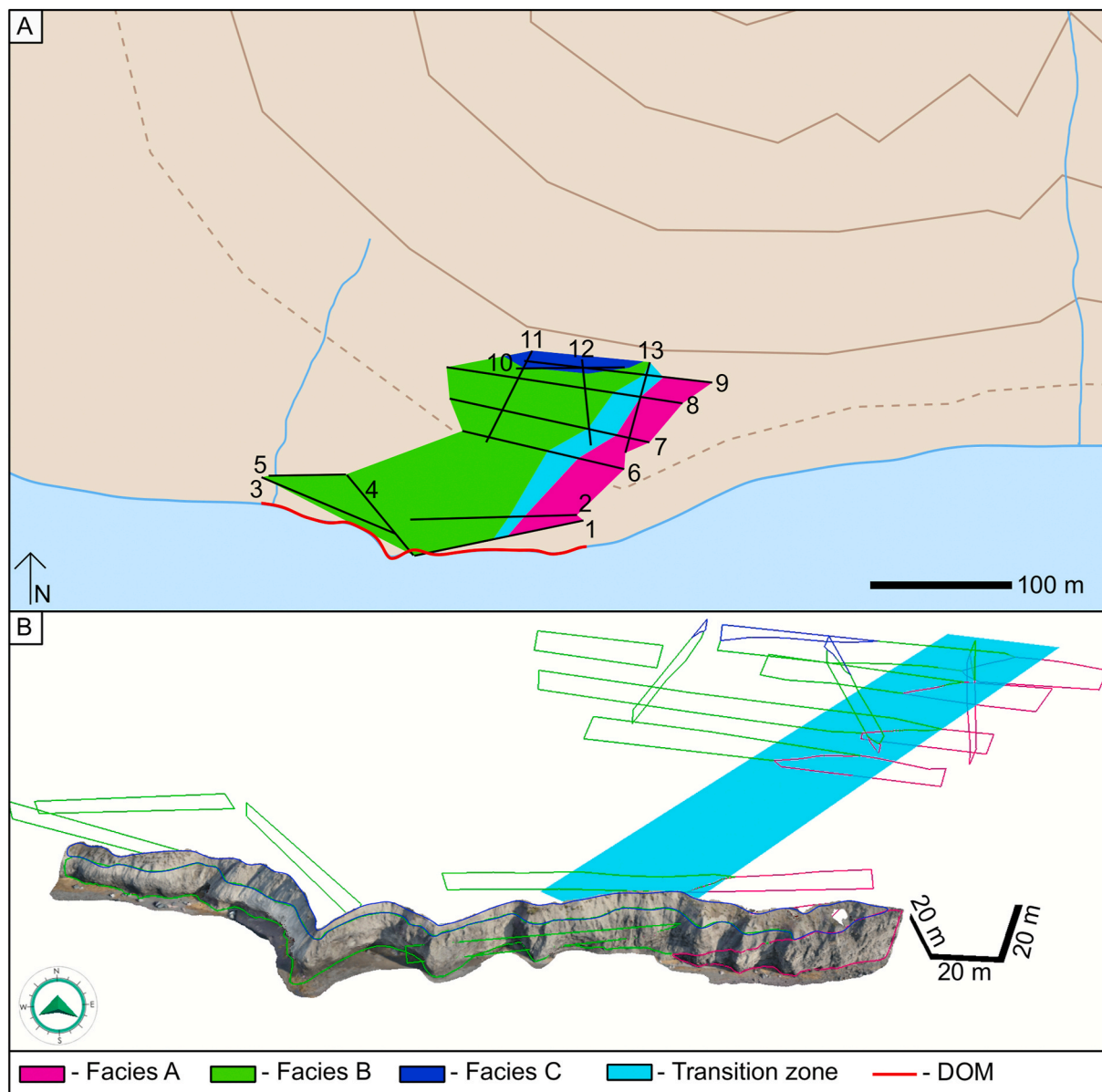


Fig. 12. Mapping the paleokarst breccia extend at Rudmosepynten. A: Map of the study area showing the extend of facies A, B and C. The paleokarst breccias form a connected body covering an area of 16 000 m². Map from Norwegian Polar Institute (2014). B: 3D view of the survey area. The interpretations of the GPR profiles are displayed together with the DOM. The boundary surface between facies A and B is extrapolated from the interpretations. (For interpretation of the references to color in this figure legend, the reader is referred to the Web version of this article.)

the subsurface behind the outcrop allows us to build 3D geo-models of paleokarst features and potentially other sedimentary structures/features observed in the outcrop, DOM and GPR. For future efforts this method could be integrated with electrical resistivity tomography and shallow seismic across a large plateaus to provide more geophysical characteristics.

With this study we have shown that the integration of detailed outcrop descriptions, DOMs and GPR directly on top of the outcrop yields the potential of a geologically driven interpretation of the DOM and GPR data. This geologically driven interpretation improves the confidence in the interpretations and the 2D GPR profiles enable us to extend our observations into the third dimension.

Carbonates and in particular karstified carbonates comprise large three-dimensional heterogeneities and are difficult to model into the subsurface behind outcrops. The link of geophysical data with outcrop data enables a better 3D geomodelling of these environments by adding about internal architecture, dimensions and composition information

beyond the outcrop.

6. Conclusion

In this contribution we have integrated shallow subsurface ground penetrating radar (GPR) data with conventional outcrop data and digital outcrop models (DOMs). By integrating these datasets, we were able to directly and indirectly link lithofacies characteristics to GPR facies reflectors. We were also able to correlate key horizons in outcrop, DOM and GPR to produce a three-dimensional geology-driven interpretation of geophysical data. This has enabled us to demonstrate a clear link between the chaotic nature of paleokarst breccias in outcrop and the highly diffracted GPR reflectors of the equivalent GPR facies. In the GPR profiles we could trace the paleokarst breccia and the paleo-cave base for 150 m beyond the outcrop. In this study we have shown that the integration of outcrop, DOM and GPR data sets have the potential to strengthen and extend the interpretation of conventional outcrop data.

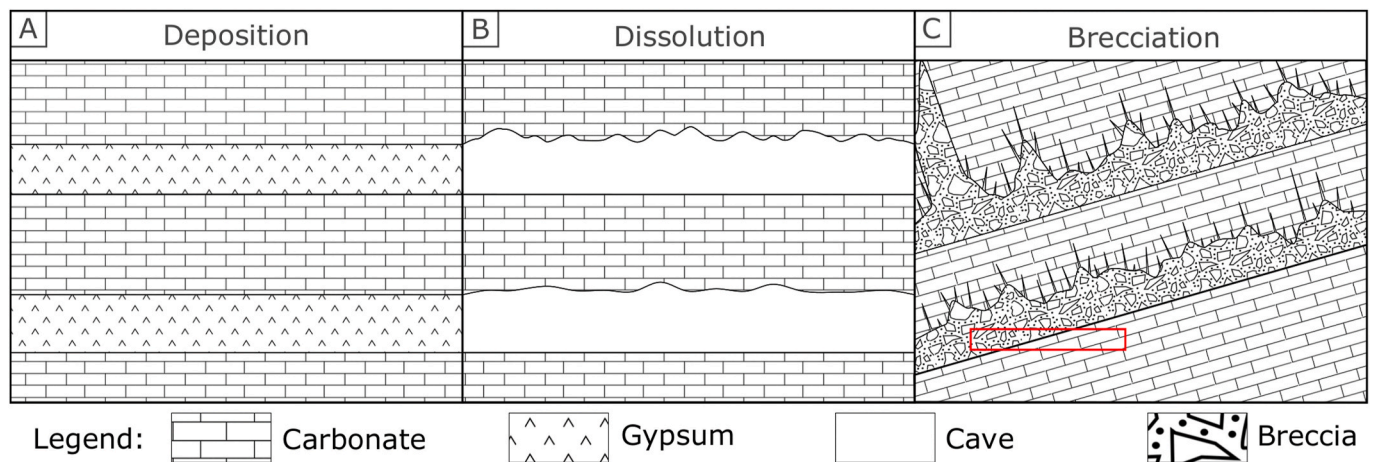


Fig. 13. Schematic cartoon showing the deposition, dissolution, and brecciation of the paleokarst succession at Fortet (Not to scale). **A:** Depositional stage, simplified stratigraphy of the Minkinfjellet Formation after deposition. Showing alternating carbonate and gypsum deposition. **B:** Dissolution stage, dissolution of the gypsum layers, showing the sharp flat base and the irregular top of the formed cavities. **C:** Brecciation stage, subsequent collapse and infill of the paleo-caves. Paleo-cave roof collapse with subsequent paleo-cave infill. Tilting of layers to better represent the Rudmosepynten outcrop. Fracturing in the overburden above the paleo-cave roof. Left side shows link to the cross-cutting breccia pipes in the Wordiekammen Formation. Red box indicates approximate location of the Rudmosepynten outcrop in the model. Brecciation model adopted from [Eliassen and Talbot \(2005\)](#), paleokarst infill inspired by [Loucks \(1999\)](#). (For interpretation of the references to color in this figure legend, the reader is referred to the Web version of this article.)

None the less detailed outcrop descriptions are essential to improve the interpretation of both DOM and GPR datasets.

CRediT author statement

Julian Janocha: Conceptualization, Data curation, Formal analysis, Funding acquisition, Fieldwork, Investigation, Methodology, Project administration, Software, Visualization, Writing – original draft, Writing – review & editing. **Aleksandra Smyrak-Sikora:** Validation, Visualization, Writing – review & editing. **Kim Senger:** Conceptualization, Funding acquisition, Resources, Supervision, Validation, Writing – review & editing. **Thomas Birchall:** Validation, Writing – review & editing.

Declaration of competing interest

The authors declare that they have no known competing financial interests or personal relationships that could have appeared to influence the work reported in this paper.

Acknowledgments

We gratefully acknowledge funding for fieldwork from the Svalbard Science Forum and the Research Council of Norway through two Arctic Field Grants (grant numbers 282547 and 296084) and from the Research Centre for Arctic Petroleum Exploration (ARCEX), which is funded by industry partners and the Research Council of Norway (grant number 228107). We also acknowledge UArctic for financing hardware (drones) and software (Agisoft Metashape) to UNIS. UNIS provided both equipment and logistical support for the field campaigns. Jan Tveranger and Walter Wheeler assisted in planning fieldwork and technical discussions. Snorre Olaussen is thanked for an extra day at the outcrop for detailed stratigraphic logging and facies descriptions. Field assistants Niklas Schaaf, Kristine Larssen, Peter Betlem and Trine Andersen provided invaluable help acquiring the data and ensuring safety during the field campaign in 2018 and in 2019. The Czech Polar field station in Petuniabukta provided boat transport to Rudmosepynten from Pyramiden. Gareth S. Lord provided valuable and constructive feedback on an earlier version of the manuscript. We would also like to thank the reviewers for their constructive feedback improving the quality of the paper and the guest-editors of the special issue on 3D modeling of

carbonates for their work.

References

- Agisoft, 2020. Agisoft Metashape Professional (Version 1.6.2) (Software). <https://www.agisoft.com/downloads/installer/>.
- Ahlborn, M., Stemmerik, L., 2015. Depositional evolution of the Upper Carboniferous – Lower Permian Wordiekammen carbonate platform, Nordfjorden High, central Spitsbergen, Arctic Norway. *Norw. J. Geol.* 95 (1), 91–126. <https://doi.org/10.17850/njg95-1-03>.
- Anderson, R.Y., Kierzke, K.K., Rhodes, D.J., 1978. Development of dissolution breccias, northern Delaware Basin. In: *New Mexico and Texas*, vol. 159. New Mexico Bureau Mines & Mineral Resources.
- Asprion, U., Aigner, T., 1999. Towards realistic aquifer models: three-dimensional georadar surveys of Quaternary gravel deltas (Singen Basin, SW Germany). *Sediment. Geol.* 129, 281–297. [https://doi.org/10.1016/S0037-0738\(99\)00068-8](https://doi.org/10.1016/S0037-0738(99)00068-8).
- Bælum, K., Braathen, A., 2012. Along-strike changes in fault array and rift basin geometry of the Carboniferous Billefjorden Trough, Svalbard, Norway. *Tectonophysics* 546–547, 38–55. <https://doi.org/10.1016/j.tecto.2012.04.009>.
- Bellian, J.A., Kerans, C., Jennette, D.C., 2005. Digital outcrop models: applications of terrestrial scanning lidar technology in stratigraphic modeling. *J. Sediment. Res.* 75, 166–176. <https://doi.org/10.2110/jsr.2005.013>.
- Bemis, S.P., Micklethwaite, S., Turner, D., James, M.R., Akciz, S., Thiele, S.T., Bangash, H.A., 2014. Ground-based and UAV-Based photogrammetry: a multi-scale, high-resolution mapping tool for structural geology and paleoseismology. *J. Struct. Geol.* 69, 163–178. <https://doi.org/10.1016/j.jsg.2014.10.007>.
- Bergh, S.G., Braathen Jr., A., Maher, H.D., 2000. Tertiary divergent thrust directions from partitioned transpression, Brøggerhalvøya, Spitsbergen. *Norw. J. Geol.* 80 (2), 63–81.
- Blatnik, M., Culver, D.C., Gabrovšek, F., Knez, M., Kogovšek, B., Kogovšek, J., Liu, H., Mayaud, C., Mihevc, A., Mulec, J., Năpăruș-Aljancić, M., Otoničar, B., Petrič, M., Pipan, T., Prelovšek, M., Ravbar, N., Shaw, T., Slabe, T., Šebela, S., Zupan Hajna, N., 2020. Late cretaceous and Paleogene paleokarsts of the northern sector of the adriatic carbonate platform. In: *Knez, M., Otoničar, B., Petrič, M., Pipan, T., Slabe, T., Blatnik, M., Culver, D.C., Gabrovšek, F., Kogovšek, B., Kogovšek, J., Liu, H., Mayaud, C., Mihevc, A., Mulec, J., Năpăruș-Aljancić, M., Prelovšek, M., Ravbar, N., Shaw, T., Šebela, S., Zupan Hajna, N. (Eds.), Karstology in the Classical Karst*. Springer, Cham, pp. 11–31.
- Blount, D.N., Moore Jr., C.H., 1969. Depositional and non-depositional carbonate breccias, chiantla quadrangle, Guatemala. *Geol. Soc. Am. Bull.* 80 (3), 429–442. [https://doi.org/10.1130/0016-7606\(1969\)80\[429:DANCBC\]2.0.CO;2](https://doi.org/10.1130/0016-7606(1969)80[429:DANCBC]2.0.CO;2).
- Braathen, A., Bælum, K., Maher, H., Buckley, S.J., 2011. Growth of extensional faults and folds during deposition of an evaporite-dominated half-graben basin; the Carboniferous Billefjorden Trough, Svalbard. *Norwegian Journal of Geology* 91 (3), 137–161.
- Braathen, A., Bergh, S.G., Maher, H.D., 1999. Application of a critical wedge taper model to the tertiary transpressional fold-thrust belt on Spitsbergen, Svalbard. *Geol. Soc. Am. Bull.* 111 (10), 1468–1485. [https://doi.org/10.1130/0016-7606\(1999\)111<1468:AOACWT>2.3.CO;2](https://doi.org/10.1130/0016-7606(1999)111<1468:AOACWT>2.3.CO;2).
- Bubeck, A.A., Vsemirnova, E.A., Jones, R.R., Wilkinson, M.W., 2011. Combining GPR and terrestrial LiDAR to produce 3D virtual outcrop models. In: *Near Surface 2011 - 17th EAGE European Meeting of Environmental and Engineering Geophysics*. Near

- Surface 2011 - 17th EAGE European Meeting of Environmental and Engineering Geophysics. EAGE Publications BV/Netherlands, Leicester, UK, 9/12/2011 - 9/14/2011.
- Buckley, S.J., Enge, H.D., Carlsson, C., Howell, J.A., 2010. Terrestrial laser scanning for use in virtual outcrop geology. *Photogramm. Rec.* 25 (131), 225–239. <https://doi.org/10.1111/j.1477-9730.2010.00585.x>.
- Buckley, S.J., Howell, J.A., Enge, H.D., Kurz, T.H., 2008. Terrestrial laser scanning in geology: data acquisition, processing and accuracy considerations. *J. Geol. Soc.* 165 (3), 625–638. <https://doi.org/10.1144/0016-76492007-100>.
- Buckley, S.J., Ringdal, K., Naumann, N., Dolva, B., Kurz, T.H., Howell, J.A., Dewez, T.J. B., 2019. LIME: software for 3-D visualization, interpretation, and communication of virtual geoscience models. *Geosphere* 15 (1), 222–235. <https://doi.org/10.1130/GES02002.1>.
- Carrivick, J., Smith, M., Quincey, D., 2016. *Structure from Motion in the Geosciences*. Wiley Blackwell, Chichester West Sussex UK, Ames Iowa, ix, p. 197.
- Chalikakis, K., Plagnes, V., Guerin, R., Valois, R., Bosch, F.P., 2011. Contribution of geophysical methods to karst-system exploration: an overview. *Hydrogeol. J.* 19 (6), 1169–1180. <https://doi.org/10.1007/s10040-011-0746-x>.
- Chamberlain, A.T., Sellers, W., Proctor, C., Coard, R., 2000. Cave detection in limestone using ground penetrating radar. *J. Archaeol. Sci.* 27, 957–994. <https://doi.org/10.1006/jasc.1999.0525>.
- Cutbill, J.L., Challinor, A., 1965. Revision of the stratigraphical scheme for the Carboniferous and Permian rocks of Spitsbergen and Bjørnøya. *Geol. Mag.* 102 (5), 418–439.
- Dallmann, W.K., 1993. Notes on the stratigraphy, extent and tectonic implications of the Minkinfjellet basin, Middle Carboniferous of central Spitsbergen. *Polar Res.* 12 (2), 153–160. <https://doi.org/10.1111/j.1751-8369.1993.tb00430.x>.
- Lithostratigraphic lexicon of Svalbard: review and recommendations for nomenclature use Upper Paleozoic to Quaternary bedrock. In: Dallmann, W.K. (Ed.), 1999. *Norsk Polarinstittutt, Tromsø*, p. 318.
- Eliassen, A., Talbot, M.R., 2003a. Diagenesis of the Mid-Carboniferous Minkinfjellet Formation, central Spitsbergen, Svalbard. *Norw. J. Geol.* 83 (4), 319–331.
- Eliassen, A., Talbot, M.R., 2003b. Sedimentary facies and depositional history of the Mid-Carboniferous Minkinfjellet Formation, central Spitsbergen, Svalbard. *Norw. J. Geol.* 83 (4), 299–318.
- Eliassen, A., Talbot, M.R., 2005. Solution-collapse breccias of the Minkinfjellet and Wordiekammen Formations, central Spitsbergen, Svalbard: a large gypsum palaeokarst system. *Sedimentology* 52 (4), 775–794. <https://doi.org/10.1111/j.1365-3091.2005.00731.x>.
- Enge, H.D., Buckley, S.J., Rotevatn, A., Howell, J.A., 2007. From outcrop to reservoir simulation model: workflow and procedures. *Geosphere* 3 (6), 469–490. <https://doi.org/10.1130/GES00099.1>.
- Faleide, J.I., Gudlaugsson, S.T., Jacquet, G., 1984. Evolution of the western Barents Sea. *Mar. Petrol. Geol.* 1 (2), 123–150. [https://doi.org/10.1016/0264-8172\(84\)90082-5](https://doi.org/10.1016/0264-8172(84)90082-5).
- Fernandes, A.L., Medeiros, W.E., Bezerra, F.H.R., Oliveira, J.G., Cazarin, C.L., 2015. GPR investigation of karst guided by comparison with outcrop and unmanned aerial vehicle imagery. *J. Appl. Geophys.* 112, 268–278. <https://doi.org/10.1016/j.jappgeo.2014.11.017>.
- Forman, S.L., Lubinski, D.J., Ingólfsson, Ó., Zeeberg, J.J., Snyder, J.A., Siegert, M.J., Matishov, G.G., 2004. A review of postglacial emergence on Svalbard, Franz Josef Land and Novaya Zemlya, Northern Eurasia. *Quat. Sci. Rev.* 23, 1391–1434. <https://doi.org/10.1016/j.quascirev.2003.12.007>.
- Friedman, G.M., 1997. Dissolution-collapse breccias and paleokarst resulting from dissolution of evaporite rocks, especially sulfates. *Carbonates Evaporites* 12 (1), 53–63.
- Haremo, P., Andresen, A., Dypvik, H., Nagy, J., Elverhøi, A., Eikeland, T.A., Johansen, H., 1990. Structural development along the Billefjorden Fault zone in the area between Kjellströmdalen and Adventdalen/Sassendalen, central Spitsbergen. *Polar Res.* 8 (2), 195–216. <https://doi.org/10.3402/polar.v8i2.d6812>.
- Harland, B.W., Cutbill, J.L., Friend, P.F., Gobbett, D.J., Holliday, D.W., Maton, P.I., Parker, J.R., Wallis, R.H., 1974. The Billefjorden Fault Zone, Spitsbergen: the long history of a major tectonic lineament. *Nor. Polarinst. Skr.* 164, 1–89.
- Harland, W.B., Anderson, L.M., Manasrah, D., 1997. *The Geology of Svalbard*. Geological Society, London, p. 529.
- Henriksen, E., Bjørnseth, H.M., Hals, T.K., Heide, T., Kiryukhina, T., Kløvjan, O.S., Larssen, G.B., Ryseth, A.E., Rønning, K., Sollid, K., Stoupakova, A., 2011a. Chapter 17 Uplift and erosion of the greater Barents Sea: impact on prospectivity and petroleum systems. *Geological Society, London, Memoirs* 35 (1), 271–281. <https://doi.org/10.1144/M35.17>.
- Holliday, D.W., Cutbill, J.L., 1972. The Ebbadalen Formation (Carboniferous), Spitsbergen. *Proc. Yorks. Geol. Soc.* 39 (1), 1–32, 1.
- Huggenberger, P., 1993. Radar facies: recognition of facies patterns and heterogeneities within Pleistocene Rhine gravels, NE Switzerland. *Geological Society, London, Special Publications* 75, 163–176. <https://doi.org/10.1144/GSL.SP.1993.075.01.10>.
- Jakobsson, M., Mayer, L., Coakley, B., Dowdeswell, J.A., Forbes, S., Fridman, B., Hodnesdal, H., Noormets, R., Pedersen, R., Rebesco, M., Schenke, H.W., Zarayskaya, Y., Accettella, D., Armstrong, A., Anderson, R.M., Bienhoff, P., Camerlenghi, A., Church, I., Edwards, M., Gardner, J.V., Hall, J.K., Hell, B., Hestvik, O., Kristoffersen, Y., Marcussen, C., Mohammad, R., Mosher, D., Nghiem, S. V., Pedrosa, M.T., Travaglini, P.G., Weatherall, P., 2012. The international bathymetric chart of the Arctic Ocean (IBCAO) version 3.0. *Geophys. Res. Lett.* 39 (12) <https://doi.org/10.1029/2012GL052219>.
- James, M.R., Chandler, J.H., Eltner, A., Fraser, C., Miller, P.E., Mills, J.P., Noble, T., Robson, S., Lane, S.N., 2019. Guidelines on the use of structure-from-motion photogrammetry in geomorphic research. *Earth Surf. Process. Landforms* 44 (10), 2081–2084. <https://doi.org/10.1002/esp.4637>.
- Janocha, J., 2020. *Structural and Depositional Evolution of the Fortet Karst Collapse Outcrop in Inner Billefjorden, central Spitsbergen, Svalbard*. Master Thesis (Unpublished). University of Potsdam, Germany, p. 109. Master Thesis (Unpublished).
- Johannessen, E.P., Steel, R.J., 1992. Mid-Carboniferous extension and rift-infill sequences in the Billefjorden Trough, Svalbard. *Norw. J. Geol.* 72 (1), 35–48.
- Jol, H.M., Smith, D.G., Meyers, R.A., 1996. *Digital Ground Penetrating Radar (GPR): A New Geophysical Tool for Coastal Barrier Research (Examples from the Atlantic, Gulf and Pacific Coasts, U.S.A.)*. *J. Coast Res.* 12, 960–968.
- Jones, R.R., Pringle, J.K., McCaffrey, K.J.W., Imber, J., Wightman, R.H., Guo, J., Long, J. J., 2011. Extending digital outcrop geology into the subsurface. In: Martinsen, O.J., Pulham, A.J., Haughton, P.D.W., Sullivan, M.D. (Eds.), *Outcrops Revitalized - Tools, Techniques and Applications*. SEPM (Society for Sedimentary Geology), Tulsa, Okla.
- Klimchouk, A., Forti, P., Cooper, A., 1996. Gypsum karst of the world: a brief overview. *Int. J. Speleol.* 25 (3–4), 159–181.
- Korus, J.T., Joekel, R.M., Tucker, S.T., 2020. Genesis of giant, bouldery bars in a Miocene gravel-bed river: Insights from outcrop sedimentology, UAS-SfM photogrammetry, and GPR. *J. Sediment. Res.* 90 (1), 27–47. <https://doi.org/10.2110/jsr.2020.3>.
- Kostic, B., Aigner, T., 2007. Sedimentary architecture and 3D ground-penetrating radar analysis of gravelly meandering river deposits (Neckar Valley, SW Germany). *Sedimentology* 54, 789–808. <https://doi.org/10.1111/j.1365-3091.2007.00860.x>.
- Lee, K., Tomasso, M., Ambrose, W.A., Bouroullec, R., 2007. Integration of GPR with stratigraphic and lidar data to investigate behind-the-outcrop 3D geometry of a tidal channel reservoir analog, upper Ferron Sandstone, Utah. *Lead. Edge* 26 (8), 994–998. <https://doi.org/10.1190/1.2769555>.
- Lønøy, A., 1995. A Mid-Carboniferous, carbonate-dominated platform, central Spitsbergen. *Norw. J. Geol.* 75 (1), 48–63.
- Loucks, R.G., 1999. Paleocave Carbonate Reservoirs: Origins, Burial-Depth Modifications, Spatial Complexity, and Reservoir Implications. *AAPG (Am. Assoc. Pet. Geol.) Bull.* 83 (11), 1795–1834.
- Loucks, R.G., Mescher, P.K., 2001. Paleocave facies classification and associated pore types in a geologic odyssey. *AAPG Southwest Section Annual Meeting*, p. 18p. Dallas, Texas papers and abstracts on CD-ROM.
- Luthi, S.M., Flint, S.S., 2014. The application of outcrop-based research boreholes for reservoir modelling: potential, challenges and pitfalls. In: Martinus, A.W., Howell, J. A., Good, T.R. (Eds.), *Sediment-Body Geometry and Heterogeneity: Analogue Studies for Modelling the Subsurface*, vol. 387. Geological Society, London, Special Publications, pp. 233–246. <https://doi.org/10.1144/SP387.6>, 1.
- Maher, H.D., Braathen, A., 2011. Løvehovden fault and Billefjorden rift basin segmentation and development, Spitsbergen, Norway. *Geol. Mag.* 148 (1), 154–170. <https://doi.org/10.1017/s0016756810000567>.
- Manby, G.M., Lyberis, N., Chorowicz, J., Thiedig, F., 1994. Post-Caledonian tectonics along the Billefjorden fault zone, Svalbard, and implications for the Arctic region. *Geol. Soc. Am. Bull.* 106 (2), 201–216. [https://doi.org/10.1130/0016-7606\(1994\)105<0201:PCTATB>2.3.CO;2](https://doi.org/10.1130/0016-7606(1994)105<0201:PCTATB>2.3.CO;2).
- Martinez, A., Kruger, J.M., Franseen, E.K., 1998. Utility of Ground-Penetrating Radar in Near-Surface, High-Resolution Imaging of Lansing-Kansas City (Pennsylvanian) Limestone Reservoir Analogs. *Midcontinent Geoscience* 43–59.
- Matapour, Z., Karlsen, D.A., Lerch, B., Backer-Owe, K., 2019. Petroleum occurrences in the carbonate lithologies of the Gohta and Alta discoveries in the Barents Sea, Arctic Norway. *Petrol. Geosci.* 25 (1), 50–70. <https://doi.org/10.1144/petgeo2017-085>.
- McCaffrey, K.J.W., Hodgetts, D., Howell, J., Hunt, D., Imber, J., Jones, R.R., Tomasso, M., Thurmond, J., Viseur, S., 2010. Virtual fieldtrips for petroleum geoscientists. In: Vining, B.A., Pickering, S.C. (Eds.), *Petroleum Geology Conference Proceedings*, pp. 19–26. <https://doi.org/10.1144/0070019>.
- McCann, A.J., Dallmann, W.K., 1996. Reactivation history of the long-lived Billefjorden Fault Zone in north central Spitsbergen, Svalbard. *Geol. Mag.* 133 (1), 63–84. <https://doi.org/10.1017/S0016756800007251>.
- McMechan, G.A., Loucks, R.G., Zeng, X., Mescher, P., 1998. Ground penetrating radar imaging of a collapsed paleocave system in the Ellenburger dolomite, central Texas. *J. Appl. Geophys.* 39 (1), 1–10. [https://doi.org/10.1016/S0926-9851\(98\)00004-4](https://doi.org/10.1016/S0926-9851(98)00004-4).
- Neal, A., Pontee, N.I., Pye, K., Richards, J., 2002. Internal structure of mixed-sand-and-gravel beach deposits revealed using ground-penetrating radar. *Sedimentology* 49, 789–804. <https://doi.org/10.1046/j.1365-3091.2002.00468.x>.
- Nemec, W., Steel, R.J., 1984. Alluvial and coastal conglomerates: Their significant features and some comments on gravelly mass-flow deposits. *Canadian Society of Petroleum Geologists* 10, 1–31.
- Nesbit, P.R., Durkin, P.R., Hugenholtz, C.H., Hubbard, S.M., Kucharczyk, M., 2018. 3-D stratigraphic mapping using a digital outcrop model derived from UAV images and structure-from-motion photogrammetry. *Geosphere* 14 (6), 2469–2486. <https://doi.org/10.1130/GES01688.1>.
- Nicolaisen, J.B., Elvebakk, G., Ahokas, J., Bojesen-Koefoed, J.A., Olausen, S., Rinna, J., Skeie, J.E., Stemmerik, L., 2019. Characterization of Upper Paleozoic organic-rich units in Svalbard: Implications for the Petroleum Systems of the Norwegian Barents Shelf. *J. Petrol. Geol.* 42, 59–78. <https://doi.org/10.1111/jpg.12724>.
- Nordeide, H.C., 2008. *Spatial Distribution and Architecture of Breccia Pipes Features at Wordiekammen, Billefjorden, Svalbard*. University of Bergen, Norway, p. 129. Unpublished Master thesis.
- Norwegian Polar Institute, 2014. *Kartdata Svalbard 1:100 000 (S100 Kartdata)/Map Data*. Norwegian Polar Institute. <https://doi.org/10.21334/npolar.2014.64533667>.
- NPD FactMaps Desktop. accessed 9.27.20. <https://factmaps.npd.no/factmaps/3.0/>.
- Onaca, A., Ardelean, A.C., Urdea, P., Ardelean, F., Sărășan, A., 2016. Genetic typologies of talus deposits derived from GPR measurements in the alpine environment of the Făgăraș Mountains. *Caparthian Journal of Earth and Environmental Sciences* 11 (2), 609–616.

- Palmer, A.N., 1991. Origin and morphology of limestone caves. *Geol. Soc. Am. Bull.* 103, 1–21.
- Pickard, N.A.H., Eilertsen, F., Hanken, N.-M., Johansen, T.A., Lønøy, A., Nakrem, H.A., Nilsson, I., Samuelsen, T.J., Somerville, J.D., Ville, E., 1996. Stratigraphic framework of Upper Carboniferous (Moscovian–Kasimovian) strata in Bunsow Land, central Spitsbergen: palaeogeographic implications. *Norw. J. Geol.* 76, 169–185.
- Pierce, C.S., Haughton, P.D.W., Shannon, P.M., Pulham, A.J., Barker, S.P., Martinsen, O. J., 2018. Variable character and diverse origin of hybrid event beds in a sandy submarine fan system, Pennsylvanian Ross Sandstone Formation, western Ireland. *Sedimentology* 65, 952–992. <https://doi.org/10.1111/sed.12412>.
- Pringle, J.K., Clark, J.D., Westerman, A.R., Gardiner, A.R., 2003. The use of GPR to image three-dimensional (3-D) turbidite channel architecture in the Carboniferous Ross Formation, County Clare, western Ireland. In: Bristow, C.S., Jol, H.M. (Eds.), *Ground Penetrating Radar in Sediments*, vol. 211. Geological Society, London, Special Publications, pp. 315–326. <https://doi.org/10.1144/GSL.SP.2001.211.01.25>, 1.
- Pringle, J.K., Howell, J.A., Hodgetts, D., Westerman, A.R., Hodgson, D.M., 2006. Virtual outcrop models of petroleum reservoir analogues: a review of the current state-of-the-art. *First Break* 24 (1093). <https://doi.org/10.3997/1365-2397.2006005>.
- Rittersbacher, A., Buckley, S.J., Howell, J.A., Hampson, G.J., Vallet, J., 2014. Helicopter-based laser scanning: a method for quantitative analysis of large-scale sedimentary architecture. In: Martinius, A.W., Howell, J.A., Good, T.R. (Eds.), *Sediment-Body Geometry and Heterogeneity: Analogue Studies for Modelling the Subsurface*, vol. 387. Geological Society, London, Special Publications, pp. 185–202. <https://doi.org/10.1144/SP387.3>, 1.
- Robinson, M., Bristow, C., McKinley, J., Ruffell, A., 2013. *Ground Penetrating Radar. Geomorphological Techniques* 1–26.
- Sandmeier, K., 2019. ReflexW (Version 9.5.1) (Software) (2020). <https://www.sandmeier-geo.de/download.html>.
- Sayago, J., Di Lucia, M., Mutti, M., Cotti, A., Sitta, A., Broberg, K., Przybylo, A., Buonaguro, R., Zimina, O., 2012. Characterization of a deeply buried paleokarst terrain in the Loppa High using core data and multiattribute seismic fades classification. *AAPG (Am. Assoc. Pet. Geol.) Bull.* 96 (10), 1843–1866. <https://doi.org/10.1306/02271211137>.
- Senger, K., Betlem, P., Birchall, T., Buckley, S.J., Coakley, B., Eide, C.H., Flaig, P.P., Forien, M., Galland, O., Gonzaga Jr., L., Jensen, M., Kurz, T., Lecomte, I., Mair, K., Malm, R.H., Mulrooney, M., Naumann, N., Nordmo, I., Ogata, K., Rabbel, O., Schaaf, N., Smyrak-Sikora, A., 2020. Using digital outcrops to make the high Arctic more accessible through the Svalbox database. *J. Geosci. Educ.* 1–15. <https://doi.org/10.1080/10899995.2020.1813865>.
- Senger, K., Tveranger, J., Wheeler, W., Braathen, A., Heincke, B., 2014. GPR characterization of a naturally fractured siliciclastic reservoir on Svalbard, Arctic Norway. In: *Proceedings of the 15th International Conference on Ground Penetrating Radar, GPR 2014* (June), pp. 285–290. <https://doi.org/10.1109/ICGPR.2014.6970430>.
- Simpson, F., 1988. Solution-Generated Collapse (SGC) Structures Associated with Bedded Evaporites: Significance to base-metal and hydrocarbon localization. *Geosci. Can.* 15 (2), 89–93.
- Smith, M.W., Carrivick, J.L., Quincey, D.J., 2016. Structure from motion photogrammetry in physical geography. *Prog. Phys. Geogr.: Earth Environ.* 40 (2), 247–275. <https://doi.org/10.1177/0309133315615805>.
- Smyrak-Sikora, A., Johannessen, E.P., Olausen, S., Sandal, G., Braathen, A., 2019. Sedimentary architecture during Carboniferous rift initiation – the arid Billefjorden Trough, Svalbard. *J. Geol. Soc.* 176 (2), 225–252. <https://doi.org/10.1144/jgs2018-100>.
- Smyrak-Sikora, A.A., 2020. Development of Extensional Growth Basins: A Field Based Study, Svalbard, Norway. PhD. University of Bergen, UNIS, Norway. <http://hdl.handle.net/1956/21496>.
- Solbakk, T., 2020. Testing karstified carbonates. *GEO Energi & Ressurser* 23 (4), 42.
- Sorento, T., Olausen, S., Stemmerik, L., 2020. Controls on deposition of shallow marine carbonates and evaporites – lower Permian Gipsbukken Formation, central Spitsbergen, Arctic Norway. *Sedimentology* 67, 207–238. <https://doi.org/10.1111/sed.12640>.
- Stemmerik, L., Worsley, D., 2005. 30 years on - Arctic Upper Paleozoic stratigraphy, depositional evolution and hydrocarbon prospectivity. *Norw. J. Geol.* 85, 151–168.
- Swennen, R., Viaene, W., Cornelissen, C., 1990. Petrography and geochemistry of the Belle Roche breccia (lower Visean, Belgium): evidence for brecciation by evaporite dissolution. *Sedimentology* 37, 859–878.
- Tian, F., Wang, Z., Cheng, F., Xin, W., Fayemi, O., Zhang, W., Shan, X., 2019. Three-Dimensional Geophysical Characterization of Deeply Buried Paleokarst System in the Tahe Oilfield, Tarim Basin, China. *Water* 11 (5), 1045. <https://doi.org/10.3390/w11051045>.
- Verba, M.L., 2013. Kollektorneye svoystva porod osadochnogo chekhka arhipelaga Shpitsbergen [Sedimentary cover reservoir of Svalbard archipelago]. *Neftegazovaya Geologiya. Teoriya I Praktika* 8. <https://doi.org/10.17353/2070-5379/5.2013>.
- Westoby, M.J., Brasington, J., Glasser, N.F., Hambrey, M.J., Reynolds, J.M., 2012. ‘Structure-from-Motion’ photogrammetry: A low-cost, effective tool for geoscience applications. *Geomorphology* 179, 300–314. <https://doi.org/10.1016/j.geomorph.2012.08.021>.
- Wheeler, W., Tveranger, J., Heincke, B., Rossi, G., Stremmerik, L., Breesch, L., Braathen, A., Maher, H., Buckley, S., 2011. A Paleokarst Collapse Breccia Pipe Reservoir Analogue, Carboniferous, Svalbard. AAPG International Conference and Exhibition, Milano, Italy, p. 1.
- Wilkinson, M.W., Jones, R.R., Woods, C.E., Gilment, S.R., McCaffrey, K.J.W., Kokkalas, S., Long, J.J., 2016. A comparison of terrestrial laser scanning and structure-from-motion photogrammetry as methods for digital outcrop acquisition. *Geosphere* 12 (6), 1865–1880. <https://doi.org/10.1130/GES01342.1>.
- Young, R.A., Slatt, R.M., Staggs, J.G., 2003. Application of ground penetrating radar imaging to deepwater (turbidite) outcrops. *Mar. Petrol. Geol.* 20 (6–8), 809–821. <https://doi.org/10.1016/j.marpetgeo.2003.01.005>.
- Zeng, H., Loucks, R., Janson, X., Wang, G., Xia, Y., Yuan, B., Xu, L., 2011. Three-dimensional seismic geomorphology and analysis of the Ordovician paleokarst drainage system in the central Tabei Uplift, northern Tarim Basin, western China. *AAPG (Am. Assoc. Pet. Geol.) Bull.* 95 (12), 2061–2083. <https://doi.org/10.1306/03111110136>.